REPORT DOCUMENTATION PAGE

Form Approved
OMB No. 0704-0188

PLEASE DO NOT RETURN YOUR FORM TO THE ABOVE ADDRESS.

1. REPORT DATE *(DD-MM-YYYY)*	2. REPORT TYPE	3. DATES COVERED *(From - To)*
March 29, 2010	Final Technical Report	February 2009 - November 2009

4. TITLE AND SUBTITLE

Nonlinear High Fidelity Aeroelastic Analysis for Novel Configurations

5a. CONTRACT NUMBER

FA9550-09-1-0066

5b. GRANT NUMBER

313-0016

5c. PROGRAM ELEMENT NUMBER

N/A

6. AUTHOR(S)

Earl H. Dowell
Deman Tang
Peter Attar

5d. PROJECT NUMBER

N/A

5e. TASK NUMBER

N/A

5f. WORK UNIT NUMBER

N/A

7. PERFORMING ORGANIZATION NAME(S) AND ADDRESS(ES)

Duke University, Mechanical Engineering and Materials Science Dept.
Pratt School of Engineering
P.O. Box 90300
Durham, NC 27708

8. PERFORMING ORGANIZATION REPORT NUMBER

N/A

9. SPONSORING/MONITORING AGENCY NAME(S) AND ADDRESS(ES)

Air Force Office of Scientific Research
875 N. Randolph Street, Suite 325
Arlington, VA 22203

10. SPONSOR/MONITOR'S ACRONYM(S)

AFOSR

11. SPONSOR/MONITOR'S REPORT NUMBER(S)

AFRL-SR-AR-TR-10-0168

12. DISTRIBUTION/AVAILABILITY STATEMENT

No Limitations

13. SUPPLEMENTARY NOTES

N/A

14. ABSTRACT

A folding wing structure consisting of three components: fuselage, inboard wing and outboard wing, is modeled computationally using a geometrically nonlinear structural dynamics theory based upon von Karman strains and at three-dimensional nonlinear potential flow aerodynamic model. The structural dynamic equations of motion are discretized in space using a discrete Ritz basis derived from finite element analysis and component synthesis and the aerodynamic model is discretized using a vortex lattice. Results from the computational model are compared to those from experiments designed and tested in the Duke University wind tunnel for three folding wing configurations. It is found that limit cycle oscillation magnitude and frequency results from theory compare well with those measured in the experiment. Also it appears that structural nonlinearities are stronger than aerodynamic nonlinearities for the cases studied.

15. SUBJECT TERMS

Aeroelasticity, morphing wings, folding wings, flutter, limit cycle oscillations, computational models, wind tunnel experiments

16. SECURITY CLASSIFICATION OF:			17. LIMITATION OF ABSTRACT	18. NUMBER OF PAGES	19a. NAME OF RESPONSIBLE PERSON
a. REPORT	b. ABSTRACT	c. THIS PAGE			19b. TELEPHONE NUMBER *(Include area code)*

Reset

Nonlinear Aeroelastic Study for Folding Wing Structures*

Peter J. Attar †

The University of Oklahoma

Deman Tang‡

Earl H. Dowell §

Duke University

A folding wing structure consisting of three components: fuselage, inboard wing and outboard wing, is modeled computationally using a geometrically nonlinear structural dynamics theory based upon von Kármán strains and a three-dimensional nonlinear potential flow aerodynamic model. The structural dynamic equations of motion are discretized in space using a discrete Ritz basis derived from finite element analysis and component synthesis and the aerodynamic model is discretized using a vortex lattice. Results from the computational model are compared to those from experiments designed and tested in the Duke University wind tunnel for three folding wing configurations. It is found that overall, limit cycle oscillation magnitude and frequency results from theory compare well with those measured in the experiment. The study also indicated that as the flow velocity is increased, the computed limit cycle response of the inboard wing showed a higher level of dynamic complexity, as measured by the number of significant frequencies contained in the response, than the experimental model. The theoretical model also predicts that, for the two folding

*An earlier version of the this paper was presented at the NATO RTO Symposium AVT-168 on Morphing Vehicles, Evora, Portugal, April 2009

†Assistant Professor, Department of Aerospace and Mechanical Engineering, 865 Asp Ave, Felgar Hall Room 212, Norman, OK 73019, Member AIAA.e-mail: peter.attar@ou.edu

‡Research Scientist, Department of Mechanical Engineering and Materials Science, Box 90300, Hudson Hall, Durham, NC 27708-0300. Member AIAA.

§Coresponding Author. William Holland Hall Professor, Department of Mechanical Engineering and Materials Science, Box 90300, Hudson Hall, Durham, NC 27708-0300. Dean Emeritus,Pratt School of Engineering, Honorary Fellow AIAA.Tel: 919- 660- 5302, fax: 919- 660- 0089, E-mail: dowell@ee.duke.edu.

wing configurations with the smaller outboard folding angles, the outboard wing limit cycle oscillation tip displacement results are very similar and significantly larger in magnitude than those of the configuration with the largest outboard folding angle. Overall both the theoretical and experimental models demonstrate that different flutter and limit cycle behavior may occur for different folding wing configurations. Also it appears that structural nonlinearities are stronger than aerodynamic nonlinearities for the cases studied.

I. Introduction

Efforts to develop morphing air vehicles with multiple mission capabilities have recently been undertaken by several research teams including NASA's Aircraft Morphing program[1] and the Defense Advanced Research Projects Agency's Morphing Aircraft Structures program.[2] One such morphing wing structure is the folding wing concept. With multiple individually articulated sections, various wing geometries can be achieved in-flight allowing for multirole missions with the same aircraft.

Several parametric studies have been performed to assess the *linear* aeroelastic characteristics of generic folding wing configurations.[3–7] The effect on aeroelastic stability of such parameters as inboard wing folding angle and hinge stiffness were investigated. Conclusions from these studies include 1)a trend of increasing flutter dynamic pressure with increasing inboard wing folding angle 2)higher sensitivity of flutter dynamic pressure with respect to outboard hinge stiffness as compared to the inboard hinge stiffness and 3) morphing wing actuation energy depends on center of gravity position, Mach number and wing sweep.

Lee and Chen[8] studied the effect of hinge free-play on the flutter and limit cycle oscillation of folding wings. They observed that, for folding angles between 0 and 30 degrees, limit cycle oscillation occurs even when the flight altitude is above that of the flutter boundary. Further increases of the folding wing angle above 30 degrees resulted in no limit cycle oscillation. They observed that when limit cycle oscillation did occur, it could occur even for very small values of the free-play parameter ($\pm 0.02^o$).

In recent work, Tang and Dowell[9] introduced the concept of using component modal analysis to model, efficiently and accurately, multi-component folding wing configurations. Their results showed that an increase in inboard wing hinge stiffness lead to improved aeroelastic stability while an increase in outboard hinge stiffness decreased the flutter velocity. They also noted that for certain values of inboard hinge stiffness a hump-type flutter could occur. Their computational results were also compared to experiment and in the experiment limit cycle oscillation was observed. Good agreement was found between computed and measured flutter velocities and frequencies. However due to the linear nature of the structural and

aerodynamic computational models used in this work, the prediction of these limit cycles was not possible.

The work presented in this paper is an extension of that presented in Ref. 9 to include nonlinear effects in both the structural and aerodynamic models. Geometric nonlinearity in the structure is modeled using von Kármán strains with Kirchhoff thin-plate theory and the resulting nonlinear variational statement is discretized with a discrete Ritz basis computed using a combined finite-element/component synthesis analysis. The flow is modeled using a vortex lattice potential model which accounts for the nonlinear tangent flow boundary conditions. Post-flutter limit cycle results from the computational model are compared to those measured in experiment for three different outboard wing folding angle configurations.

II. Folding Wing Configuration

A schematic of the folding wing geometry which is to be investigated is shown in Figure 1. The folding wing system consists of three separate components, component A, i.e. fuselage; component B , i.e. inboard wing and component C , i.e. outboard wing. Components A and B are attached through a hinge which is modeled as a set of torsional springs at several points, P_j with spring stiffness, K_{Aj}. Components B and C are also attached through a hinge which is modeled as a set of torsional springs at several points, S_j with torsional spring stiffness, K_{Bj}. The hinge model is assumed to have negligible mass compared to the wing structure model. The initial folding angles between components A and B, and B and C are θ_b and θ_c, respectively. Note that θ_b and θ_c are the static equilibrium angles. These depend upon the initial unsprung wing folding angle and sprung deformation due to wing gravity. In addition to the main coordinate system, xyz, two additional local coordinate systems, $\zeta_b\eta_b\xi_b$ and $\zeta_c\eta_c\xi_c$ for components B and C are used as shown in Figure 1.

The relationships between the main coordinate system and local coordinate systems are expressed as follows.

$$\left\{\begin{array}{c} x \\ y \\ z \end{array}\right\}_B = \left\{\begin{array}{c} l_A \tan\beta_0 \\ l_A \\ 0 \end{array}\right\} + \left[\begin{array}{ccc} 1 & 0 & 0 \\ 0 & \cos\theta_B & -\sin\theta_B \\ 0 & \sin\theta_B & \cos\theta_B \end{array}\right] \left\{\begin{array}{c} \zeta \\ \eta \\ \xi \end{array}\right\}_B \tag{1}$$

$$\left\{\begin{array}{c} x \\ y \\ z \end{array}\right\}_C = \left\{\begin{array}{c} (l_A + l_B\cos\theta_B)\tan\beta_0 \\ l_A + l_B\cos\theta_B \\ l_B\sin\theta_B \end{array}\right\} + \left[\begin{array}{ccc} 1 & 0 & 0 \\ 0 & \cos\theta_C & -\sin\theta_C \\ 0 & \sin\theta_C & \cos\theta_C \end{array}\right] \left\{\begin{array}{c} \zeta \\ \eta \\ \xi \end{array}\right\}_C .$$

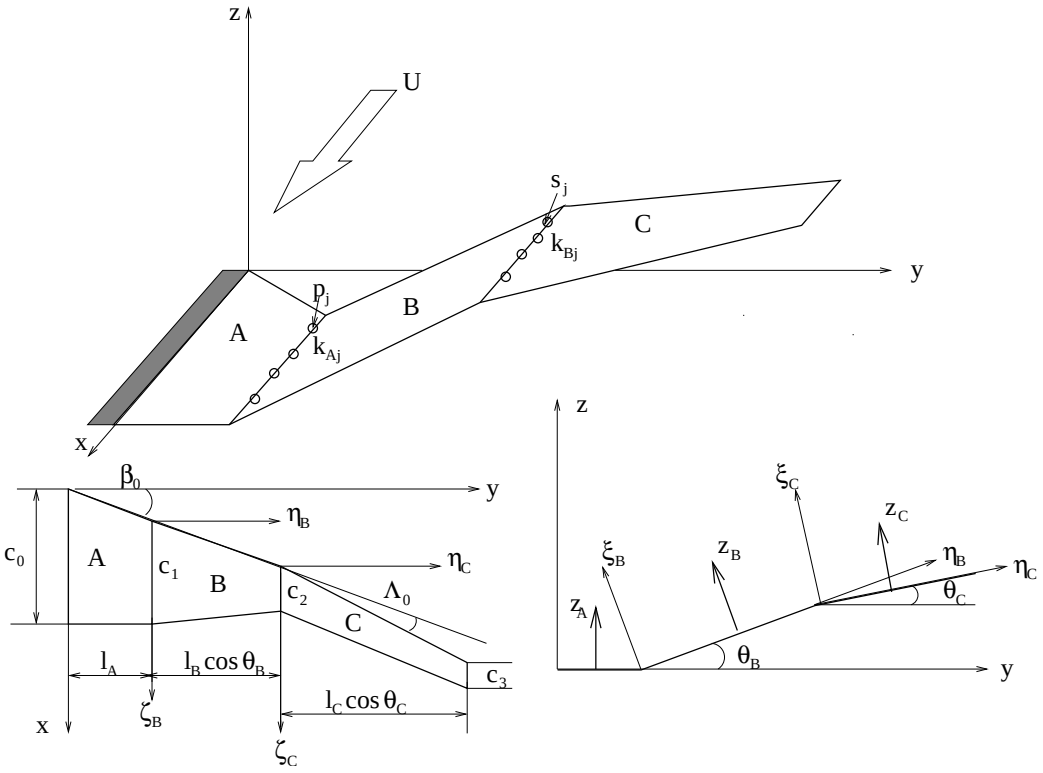

Figure 1. Schematic of a folding wing geometry and coordinate systems.

III. Structural Equations of Motion

A. Nonlinear Variational Statement

The statement of virtual work requires that the work done by externally applied loads be equal to the work done by inertial, dissipative and internal forces for any virtual displacement. For a structure with volume V and surface area S this can be written as

$$\int_V \delta\mathbf{u}^T\mathbf{F}dV + \int_S \delta\mathbf{u}^T\mathbf{\Phi}_{tr}dS = \int_V \left(\delta\mathbf{u}^T\rho\ddot{\mathbf{u}} + \delta\mathbf{u}^T c\dot{\mathbf{u}} + \delta\boldsymbol{\epsilon}^T\boldsymbol{\sigma}\right)dV \ , \tag{2}$$

where $\mathbf{F}$ and $\mathbf{\Phi}_{tr}$ represent prescribed body forces and surface tractions, ρ is the mass density and c is a damping parameter. Also $\delta\mathbf{u}$, $\delta\boldsymbol{\epsilon}$ and $\boldsymbol{\sigma}$ represent the vectors of virtual displacements, virtual Green-Lagrange strains and second Kirchhoff-Piola stresses respectively.

Here it will be assumed that Kirchhoff plate theory applies and that plate rotations are negligible compared to unity (von Kármán assumption). With these simplifications, the

Green-Lagrange strains can be written as

$$\epsilon_{xx} = \hat{u}_x + \frac{1}{2}\hat{w}_x^2 - z\hat{w}_{xx} \tag{3}$$

$$\epsilon_{yy} = \hat{v}_y + \frac{1}{2}\hat{w}_y^2 - z\hat{w}_{yy} \tag{4}$$

$$\epsilon_{xy} = \hat{u}_y + \hat{v}_x + \hat{w}_x\hat{w}_y - 2z\hat{w}_{xy} \ , \tag{5}$$

where to the degree of accuracy given by the von Kármán and Kirchhoff assumptions, the x, y and z displacements u,v and w, which make up the vector $\mathbf{u}$ in Eq. 2, are given as:

$$u \approx \hat{u} - z\frac{\partial \hat{w}}{\partial x} \tag{6}$$

$$v \approx \hat{v} - z\frac{\partial \hat{w}}{\partial y} \tag{7}$$

$$w \approx \hat{w} \ . \tag{8}$$

The displacement vector $\mathbf{u}$ now can be considered to contain only the mid-plane displacements $\hat{u}$, $\hat{v}$ and $\hat{w}$.

To be consistent with the Kirchhoff and von Kármán assumptions it is assumed that the constitutive model is linear, plane stress. Hence, given a constant component thickness h, we can define the membrane ($\mathbf{N}$) and bending ($\mathbf{M}$) resultant forces as:

$$\mathbf{N} = \int_{-h/2}^{h/2} \boldsymbol{\sigma} dz = \int_{-h/2}^{h/2} \mathbf{C}\boldsymbol{\epsilon} dz = \int_{-h/2}^{h/2} \mathbf{C}\left(\boldsymbol{\epsilon}_m + z\boldsymbol{\chi}\right) dz = h\mathbf{C}\boldsymbol{\epsilon}_m \tag{9}$$

$$\mathbf{M} = \int_{-h/2}^{h/2} \boldsymbol{\sigma} z dz = \int_{-h/2}^{h/2} \mathbf{C}\boldsymbol{\epsilon} z dz = \int_{-h/2}^{h/2} \mathbf{C}\left(\boldsymbol{\epsilon}_m + z\boldsymbol{\chi}\right) z dz = \frac{h^3}{12}\mathbf{C}\boldsymbol{\chi} \ , \tag{10}$$

where $\boldsymbol{\sigma} = \mathbf{C}\boldsymbol{\epsilon}$ is the linear plane stress constitutive relation and $\boldsymbol{\epsilon}_m$ and $\boldsymbol{\chi}$ are the membrane strains and curvatures respectively (see Eqs. 3-5).

Integrating the volume integrals in Eq. 2 over the thickness and substituting Eqs. 9, 10 gives the following virtual work expression:

$$h\int_S \delta\mathbf{u}^T\mathbf{F}dS + \int_S \delta\mathbf{u}^T\boldsymbol{\Phi}_{tr}dS = h\int_S \delta\mathbf{u}^T\rho\ddot{\mathbf{u}}dS + h\int_s \delta\mathbf{u}^T c\dot{\mathbf{u}}dS + \int_S \delta\boldsymbol{\epsilon}_m^T\mathbf{N}dS + \int_S \delta\boldsymbol{\chi}^T\mathbf{M}dS \ . \tag{11}$$

At this point a decision must be made as to how Eq. 11 is to be semi-discretized in space. In other words, what sort of trial functions (Ritz basis) will be used to represent the displacements contained in the displacement vector $\mathbf{u}$ and the variation of this vector $\delta\mathbf{u}$. Popular choices include hat functions (in finite element methods) and eigenfunctions of the

linearized system. Here we will choose these functions to be N-dimensional vectors derived using component synthesis analysis in combination with finite element analysis (to be more fully explained in the next section).

The displacement vector $\mathbf{D}$ corresponding to the x,y and z mid-plane displacements at N discrete points in space and the variation of this displacement vector $\delta\mathbf{D}$ can now be written respectively as

$$\mathbf{D} = \mathbf{\Psi}\boldsymbol{\zeta}(t) \ , \tag{12}$$

and

$$\delta\mathbf{D} = \mathbf{\Psi}\delta\boldsymbol{\zeta} \ , \tag{13}$$

where $\mathbf{\Psi}$ is a $3N \times P$ matrix containing the P $3N$-dimensional basis vectors and $\boldsymbol{\zeta}$ is a vector of independent generalized time dependent degrees of freedom. Note, if instead of finite element analysis, continuous functions were used in the component synthesis procedure, N would be equal to one.

Each basis vector in $\mathbf{\Psi}$ satisfies the system geometric boundary conditions (in the discrete sense) but not necessarily the natural boundary conditions and hence these vectors can be considered to be in the admissible class.[10]

The vectors of membrane strains and curvatures and virtual membrane strains and curvatures are expressed in terms of the generalized displacements and virtual displacements as (using standard "B matrix" notation[11]):

$$\boldsymbol{\epsilon}_m = \left(\mathbf{B}_m^l + \overline{\mathbf{B}}_m^{nl}\right)\boldsymbol{\zeta} \tag{14}$$

$$\delta\boldsymbol{\epsilon}_m = \left(\mathbf{B}_m^l + \mathbf{B}_m^{nl}\right)\delta\boldsymbol{\zeta} \tag{15}$$

$$\boldsymbol{\chi} = \mathbf{B}_b\boldsymbol{\zeta} \tag{16}$$

$$\delta\boldsymbol{\chi} = \mathbf{B}_b\delta\boldsymbol{\zeta} \ . \tag{17}$$

Substitution of Eqs. 13-17 into Eq. 11 gives:

$$\delta\boldsymbol{\zeta}^T\left(h\int_S \mathbf{\Psi}^T\mathbf{F}dS + \int_S \mathbf{\Psi}^T\mathbf{\Phi}_{tr}dS - h\int_S \mathbf{\Psi}^T\mathbf{\Psi}\rho dS\ddot{\boldsymbol{\zeta}} - h\int_S \mathbf{\Psi}^T c\mathbf{\Psi}dS\dot{\boldsymbol{\zeta}}\right.$$
$$\left. - \int_S (\mathbf{B}_m^l)^T\mathbf{N}dS - \int_S (\mathbf{B}_m^{nl})^T\mathbf{N}dS - \int_S \mathbf{B}_b^T\mathbf{M}dS\right) = 0 \ . \tag{18}$$

Considering the arbitrariness of the virtual generalized displacements, Eq. 18 can be written

as:

$$h\int_S \mathbf{\Psi}^T\mathbf{\Psi}\rho dS\ddot{\boldsymbol{\zeta}} + h\int_S \mathbf{\Psi}^T c\mathbf{\Psi}dS\dot{\boldsymbol{\zeta}} + \int_S (\mathbf{B}_m^l)^T\mathbf{N}dS + \int_S (\mathbf{B}_m^{nl})^T\mathbf{N}dS +$$
$$\int_S \mathbf{B}_b^T\mathbf{M}dS = h\int_S \mathbf{\Psi}^T\mathbf{F}dS + \int_S \mathbf{\Psi}^T\mathbf{\Phi}_{tr}dS \ . \tag{19}$$

Equation 19 is the semi-discretized (in space) equation of motion for the system. The integrals over dS in Eq. 19 are performed for each component using the midpoint rule in the local coordinate system of the component. In order to compute the derivatives needed to construct the "B" matrices in Eq. 19, third-order finite difference approximations are used.

Discretization in time of Eq. 19 is accomplished through the use of the Hilbert-Hughes-Taylor (HHT) implicit, second order, finite difference scheme.[11]

B. Derivation of Ritz Basis Through Component Synthesis

As the details of component modal synthesis are presented in great detail in many references (see Refs. 9, 10, 12–18),the general homogeneous disjoint set of equations for M components will be given without derivation. This set of disjoint equations is generated by writing Lagrange's equations for each of the components and when put into one matrix system can be expressed as

$$\mathbf{M}_d\ddot{\boldsymbol{\zeta}}_d + \mathbf{C}_d\dot{\boldsymbol{\zeta}}_d + \mathbf{K}_d\boldsymbol{\zeta}_d = \mathbf{0} \ , \tag{20}$$

where $\boldsymbol{\zeta}_d = [\boldsymbol{\zeta}_1^T, \boldsymbol{\zeta}_2^T ... \boldsymbol{\zeta}_M^T]$ is the disjoint generalized displacement vector of dimension R and $\mathbf{M}_d$,$\mathbf{C}_d$ and $\mathbf{K}_d$ are the $R \times R$ block-diagonal disjoint mass, damping and stiffness matrices respectively. The word disjoint is used here to describe a set of coordinates which are not independent. The value of R corresponds to the sum of the number of basis vectors chosen for each component. After the component (vector) bases are generated using finite element discretization, the disjoint matrices in Eq. 20 are computed using numerical integration (midpoint rule) over each component area (for the in-plane stiffness matrices) and orthonormality (for the out-of-plane stiffness matrices). Inertial contributions are considered for each component of the displacement.

In the current work, the potential energy expressions used to derive Eqs. 20 include contributions from the linear plate bending and membrane strain energy and the energy due to the torsional springs at the attachment points. The potential energy U due to these

springs, at the interfaces $A-B$ and $B-C$ (see Fig. 1), is given by

$$\begin{cases} U_{A-B} = \frac{1}{2}\sum_j K_{Aj}(\frac{\partial \hat{w}_A}{\partial y}|_{y=l_A} - \frac{\partial \hat{w}_B}{\partial \eta_B}|_{\eta_B=0})^2 & , \quad j = 1.....N_P \\ U_{B-C} = \frac{1}{2}\sum_j K_{Bj}(\frac{\partial \hat{w}_B}{\partial \eta_B}|_{\eta_B=l_B} - \frac{\partial \hat{w}_C}{\partial \eta_C}|_{\eta_C=0})^2 & , \quad j = 1.....N_S \ , \end{cases}$$

where N_P and N_S are the total numbers of the attachment points of the two interfaces.

The individual component generalized displacement vectors $\boldsymbol{\zeta}_i$ can in turn be written as

$$\boldsymbol{\zeta}_i^T = [\mathbf{a}_i^T, \mathbf{b}_i^T, \mathbf{q}_i^T] \ , \tag{21}$$

where $\mathbf{a}_i$, $\mathbf{b}_i$ and $\mathbf{b}_i$ are the ith component generalized coordinates corresponding to the vectors of x,y and z mid-plane displacements respectively:

$$\hat{\mathbf{u}}^i = \sum_j a_j^i \boldsymbol{\psi}_j^i \tag{22}$$

$$\hat{\mathbf{v}}^i = \sum_j b_j^i \boldsymbol{\eta}_j^i \tag{23}$$

$$\hat{\mathbf{w}}^i = \sum_j q_j^i \boldsymbol{\gamma}_j^i \ . \tag{24}$$

In Eqs. 22-24, $\boldsymbol{\psi}_j^i$,$\boldsymbol{\eta}_j^i$ and $\boldsymbol{\gamma}_j^i$ correspond to the jth basis vector used to expand the ith component x,y and z mid-plane displacement vectors.

In this paper the $S = 3N_p + 3N_s$ interface constraints are enforced through the writing of a matrix equation of dimension $S \times R$ which is written as

$$\mathbf{A}\boldsymbol{\zeta}_d = \mathbf{0} \ . \tag{25}$$

In order to remove the redundant coordinates from $\boldsymbol{\zeta}_d$ a coordinate transformation between $\boldsymbol{\zeta}_d$ and the set of independent coordinates $\boldsymbol{\zeta}$ is performed. This transformation is given by the equation

$$\boldsymbol{\zeta}_d = \mathbf{T}\boldsymbol{\zeta} \ . \tag{26}$$

This coordinate transformation consists of finding a basis for the null space of the matrix $\mathbf{A}$ and then expanding $\boldsymbol{\zeta}_d$ in these vectors. The basis is computed using a singular value decomposition of the matrix $\mathbf{A}$. It should be noted that an alternative method of handling the constraints would be through the introduction of Lagrange multipliers into Lagrange's equations.[12]

In the above expression for the disjoint equations of motion, the coordinate transfor-

mation between the $3N$ dimensional vector of physical displacements $\mathbf{D}$ and $\boldsymbol{\zeta}_d$ is given by

$$\mathbf{D} = \boldsymbol{\Omega}\boldsymbol{\zeta}_d \ , \tag{27}$$

where $\boldsymbol{\Omega}$ is a matrix composed of all the component basis vectors. Using the coordinate transformation given in Eq. 26, Eq. 27 can be written as

$$\mathbf{D} = \boldsymbol{\Omega}\mathbf{T}\boldsymbol{\zeta} = \boldsymbol{\Psi}\boldsymbol{\zeta} \ . \tag{28}$$

The matrix of global basis vectors $\boldsymbol{\Psi}$ is then used in the nonlinear variational statement, Eq. 19.

A further reduction in dimension can be performed if Eq. 26 is placed into Eq. 20 and the system is then premultiplied by the transpose of $\mathbf{T}$.[19] The resulting system can then be cast as an eigevalue problem and the matrix of eigenmodes $\boldsymbol{\Gamma}$ then used in the coordinate transformation:

$$\mathbf{D} = \boldsymbol{\Omega}\mathbf{T}\boldsymbol{\Gamma}\boldsymbol{\zeta}_r = \boldsymbol{\Psi}_r\boldsymbol{\zeta}_r \ . \tag{29}$$

While this procedure can lead to a drastically reduced system dimension, unfortunately the resulting global basis vectors satisfy (in the discrete sense) the linear natural in-plane boundary conditions which degrades the solution convergence of the nonlinear problem with respect to the required number of basis functions.[20]

C. Component Basis Selection

The components of the folding wing structure studied here have the following material/geometric properties. Component A is constructed from plexiglas with a modulus 3.05×10^9 Pa., density 1145 kg/m^3, Poisson's ratio of 0.45 and thickness 0.00238 m. Components B and C are constructed from aluminum with modulus 7.2×10^{10} Pa., density 2850 kg/m^3, Poisson's ratio 0.3 and thickness 0.000254 m. The stiffness values K_{Aj}, K_{Bj} used for the torsional springs at the component interfaces is 0.18 kg·m/s^2. For the results presented in this work, the value of θ_b is 30 degrees and three values of θ_c are investigated, 0, 30 and 60 degrees.

The interface constraints (as expressed in Eq. 25) are that the component mid-plane deflections ($\hat{u}$, $\hat{v}$, $\hat{w}$) in the global xyz coordinate system are to be the same at the hinge attachment points.

Each of the component bases used in this work are computed using a finite element modal analysis. The commercial code ANSYS[21] is used for this purpose. The following types of component bases are used to expand the out-of-plane deflections $\hat{\mathbf{w}}$:

Component A: the elastic out-of-plane clamped-free-free-free modes from a modal analysis of Component A.
Component B: the out-of-plane elastic and rigid body modes from a free-free-free-free modal analysis of Component B.
Component C: the out-of-plane elastic and rigid body modes from a free-free-free-free modal analysis of Component C.

The component in-plane deflections are expanded using the following types:

Component A: both $\hat{\mathbf{u}}$ and $\hat{\mathbf{v}}$ are expanded using the elastic out-of-plane simply-supported-free-free-free modes computed with a modal analysis of component A.
Component B: both $\hat{\mathbf{u}}$ and $\hat{\mathbf{v}}$ are expanded using the 3 rigid body modes from a linear plane stress modal analysis of component B and the remaining basis vectors are the elastic out-of-plane free-free-free-free modes for component B
Component C: both $\hat{\mathbf{u}}$ and $\hat{\mathbf{v}}$ are expanded using the 3 rigid body modes from a linear plane stress modal analysis of component C and the remaining basis vectors are the elastic out-of-plane free-free-free-free modes

The number of out-of-plane modes used for components A, B and C is 25, 75 and 75 respectively while the number of in-plane modes is 5, 15 and 15. These choices , after the redundant coordinates are eliminated, give a total number of structural degrees of freedom of 221. A convergence study showed that this number of modes gave a good solution convergence.

It should be noted that the choice of the types of bases used in the expansion of the in-plane components is guided by the work presented in Ref. 20.

The results for the first five modal frequencies for the three outboard wing folding configurations are shown in Table 1 (denoted as Theory in Table 1) along with the corresponding results from an ANSYS modal analysis conducted using a finite element discretization of the complete structure and experiment.

IV. Aerodynamic Equations

The flow field about the folding wing model is assumed to be potential flow. Therefore the equations of motion for the fluid can be reduced to Laplace's equation for the velocity

		$\theta_c = 0$			$\theta_c = 30$			$\theta_c = 60$	
Mode	Present Theory	ANSYS	Test	Present Theory	ANSYS	Test	Present Theory	ANSYS	Test
1	4.67	4.66	4.75	4.53	4.54	4.25	4.67	4.67	4.0
2	16.67	16.82	16.0	17.01	17.18	17.25	16.67	16.77	15.25
3	22.23	22.88	32.5	36.40	37.04	31.50	22.22	22.50	23.50
4	41.72	42.15	43.75	43.39	43.63	46.25	41.71	41.80	47.5
5	66.17	67.68	75.25	67.99	69.45	73.25	66.15	67.19	75.25

Table 1. Comparison of first five folding wing modal frequencies.

potential Φ

$$\nabla^2\Phi = 0 \ . \tag{30}$$

The boundary conditions which must be satisfied are those of zero normal flow on the wing,i.e.

$$(\nabla\Phi + \mathbf{q}) \cdot \mathbf{n} = 0 \ , \tag{31}$$

and also that the disturbance created by the potential must decay at distances far from the wing. The latter equation can be expressed as

$$\lim_{r\to\infty} \nabla\Phi = 0 \ . \tag{32}$$

In Eq. 31 $\mathbf{q}$ is the relative velocity between the undisturbed fluid in the fluid domain and the wing. Using Green's identity it can be shown[22] that a solution to Eqs. 30-32 can be found by distributing elementary solutions to Laplace's equation on the problem boundaries. For the model presented here this is accomplished by distributing vortex rings on the wing surface and in the wake.

In this work the small disturbance assumption is not made and hence the aerodynamic grid used to define bound collocation and vortex locations is moved in three dimensions using the three components of the displacment vector. It was determined through preliminary calculations that imposing the physically correct, but numerically expensive force-free wake condition had very little effect on the solution (see Fig. 2) hence the results presented here use a planar wake assumption. However the trailing edge wake shedding location is taken to be the deformed position. See Katz and Plotkin[23] for further details on the use of vortex rings to discretize the flow model.

The pressure on the wing p, which is the external load acting on the structure and used to

compute $\mathbf{\Phi}_{tr}$ in Eq. 19, is calculated using the unsteady (and nonlinear) form of Bernoulli's equation:

$$\frac{p_\infty - p}{\rho_\infty} = \frac{(\nabla\Phi)^2}{2} - \mathbf{q}\cdot\nabla\Phi + \frac{\partial\Phi}{\partial t} \ , \tag{33}$$

where p_∞ and ρ_∞ are the free stream pressure and density respectively. The time derivative in Eq. 33 is computed using a first-order backward difference approximation.

V. Coupling of Structural and Fluid Models

Coupling of the aerodynamics to the structural dynamics occurs through the specification of the tractions $\mathbf{\Phi}_{tr}$ in Eq. 19 and by the resulting structural deflection and velocity , which is used in the solution of Eqs. 30, 31.

Strong coupling of the fluid and structural models is achieved via subiteration within each timestep of the simulation.[24] As the grid used in the computation of the component bases is not coincident with the grid used in defining the aerodynamic collocation points, the tractions, structural displacements and structural velocities are interpolated using local bilinear interpolation.[25]

VI. Theoretical and Experimental Correlations

The results presented in this section are computed using the following numerical parameters. The number of chordwise aerodynamic bound vortex rings is 30 and the number spanwise bound vortex rings is 33. A total of 114 panels are used in the chordwise direction for the wake. With a timestep of 0.0005 seconds and a minimum flow velocity investigated of 15.00 m/s, this corresponds to a minimum of 3 chord lengths of wake. Structural damping is not used in the simulation, however numerical damping is present in the HHT scheme. The damping parameter in the HHT scheme is chosen to be 0.05 which has been found to give good results for nonlinear problems.[26,27] All response results shown in this section are for the structural deflection/velocity in the global z coordinate direction.

Figures 2-4 compare the inboard wing (Component B), trailing edge tip root-mean square velocity of the limit cycle oscillations (LCO) from the current computational model to those measured in the wind-tunnel experiments. Results for three different folding wing configurations are presented. For each of the configurations, the correlation between computed and measured resonse at this point on the folding wing is good. It does appear, however, that the computational model slightly underpredicts the point of bifurcation ("flutter velocity"). The computational model predicts flutter velocities of 15.5 m/s,15.35 m/s and 15.8 m/s for the configurations corresponding to $\theta_c = 0$,$\theta_c = 30$ and $\theta_c = 60$ respectively. While difficult

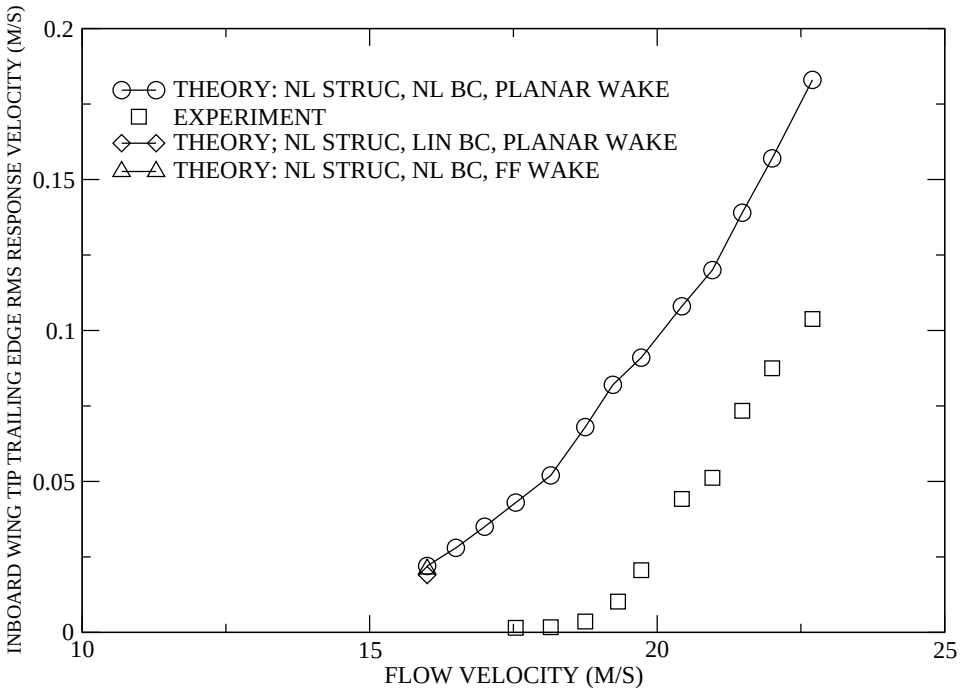

Figure 2. Component B trailing edge,tip root-mean square LCO velocity versus flow velocity; $\theta_b = 30$,$\theta_c = 0$.

to determine exactly, the flutter velocities in the experiment for these configurations are approximately 18 m/s,17.5 m/s and 17 m/s.

Also shown in Fig. 2 is a computation, for a flow velocity of 16 m/s, which includes an aerodynamic model which uses both the exact nonlinear tangent flow boundary condition and the imposition of the force-wake free condition (denoted as THEORY: NL STRUC, NL BC, FF WAKE in the figure) and a computation at 16 m/s which uses the linearized tangent flow boundary condition and a planar wake(denoted as THEORY: NL STRUC, LIN BC, PLANAR WAKE in the figure). While a definite conclusion can only be drawn for the flow velocity of 16 m/s and $\theta_b = 30$,$\theta_c = 0$ folwing wing configuration, it appears that for the stated flow velocity and folding wing configuration,including the nonlinear boundary condition in the model appears to have a slight effect while the inclusion of the force-free wake model has minimal effect. Results presented in the remainder of this section are computed using a model which includes a nonlinear structural model, the exact nonlinear tangent flow boundary condition and a planar wake assumption.

A comparison of the theoretical and experimental LCO dominant response frequencies as a function of the flow velocity, as computed from a discrete Fourier transform of the response time history, is shown in Figs. 5-7. For each of the configurations, near the flutter velocity

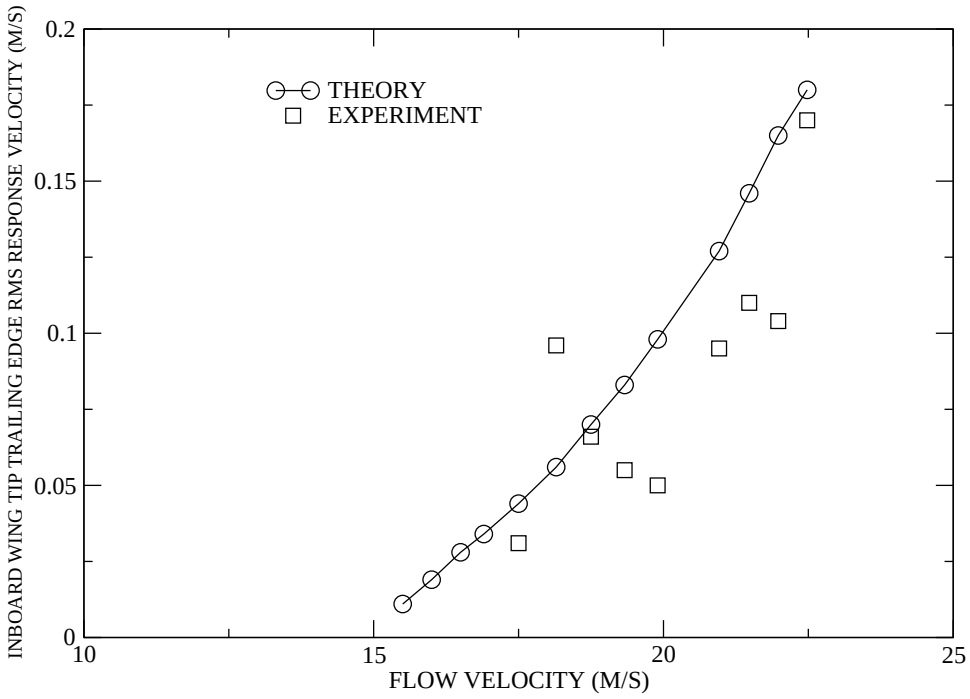

Figure 3. Component B trailing edge,tip root-mean square LCO velocity versus flow velocity; $\theta_b = 30$,$\theta_c = 30$**.**

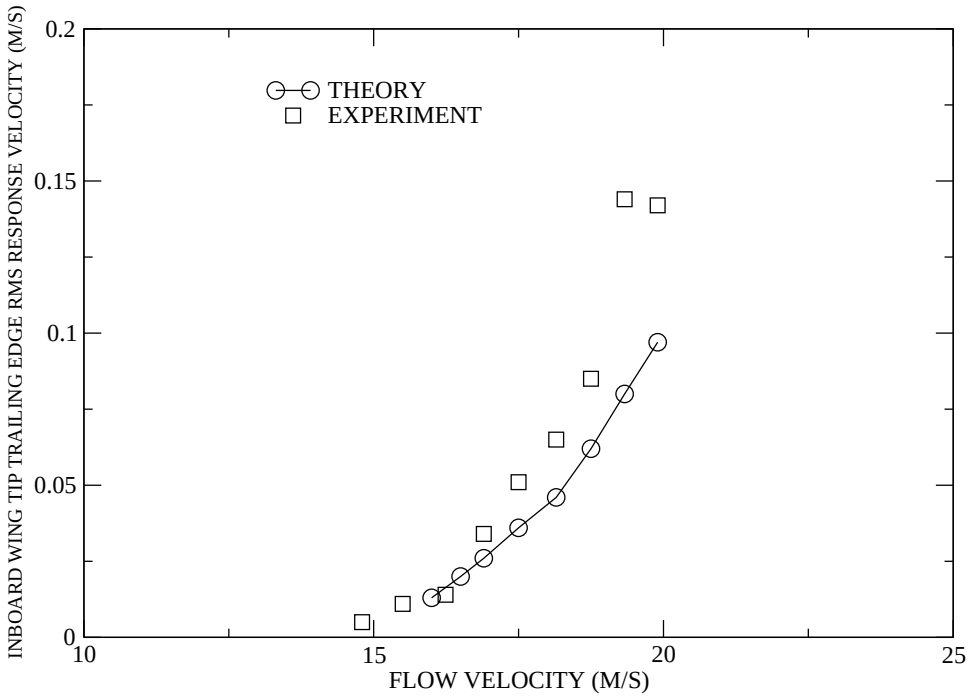

Figure 4. Component B trailing edge,tip root-mean square LCO velocity versus flow velocity; $\theta_b = 30$,$\theta_c = 60$**.**

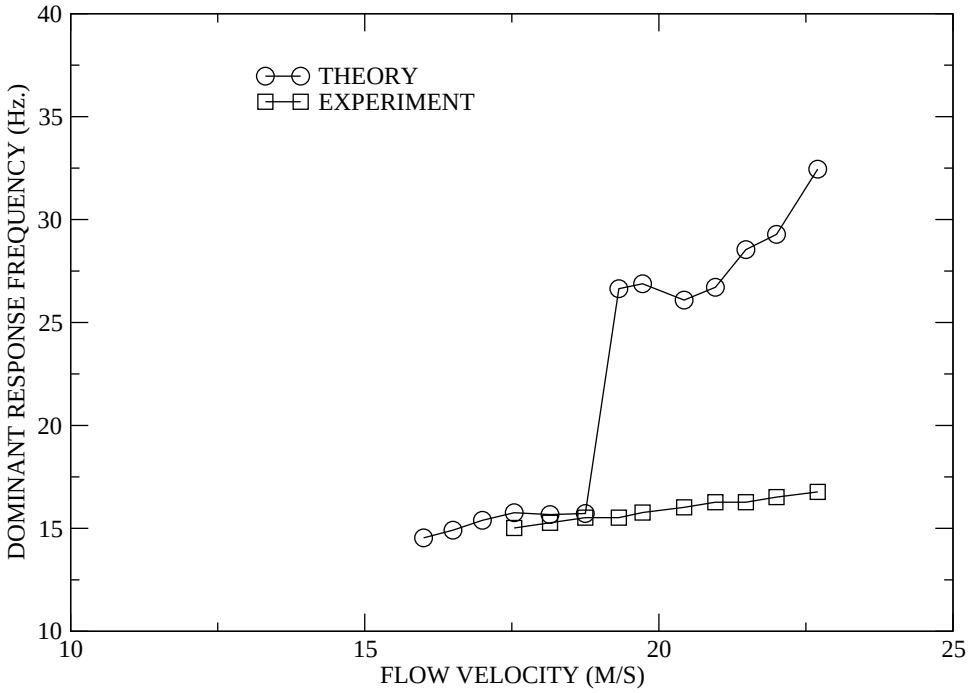

Figure 5. LCO dominant response frequency for component B trailing edge tip velocity versus flow velocity; $\theta_b = 30$,$\theta_c = 0$.

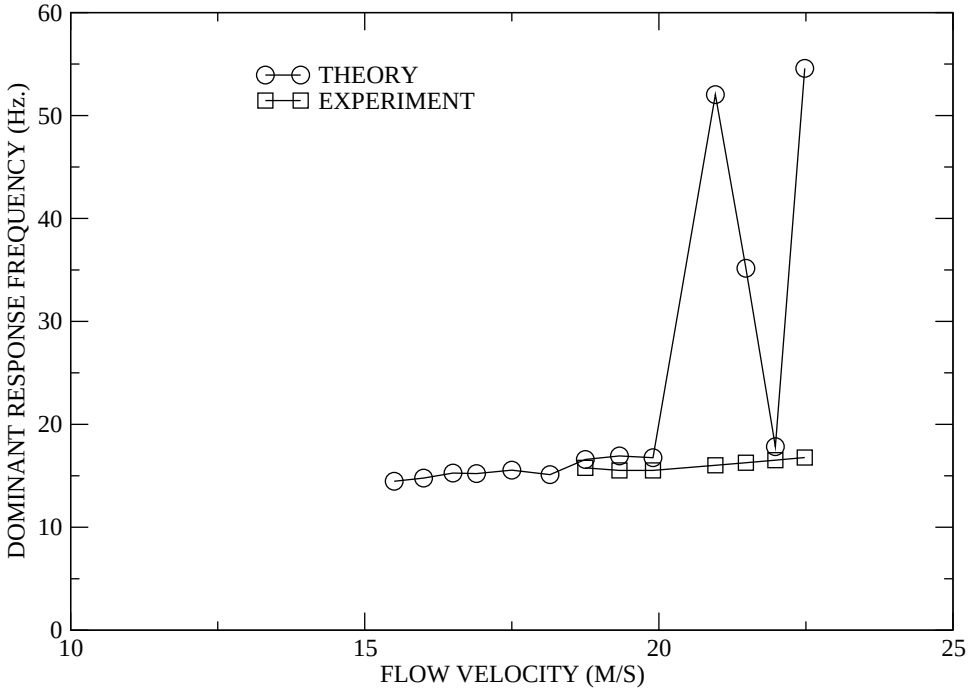

Figure 6. LCO dominant response frequency for component B trailing edge tip velocity versus flow velocity; $\theta_b = 30$,$\theta_c = 30$.

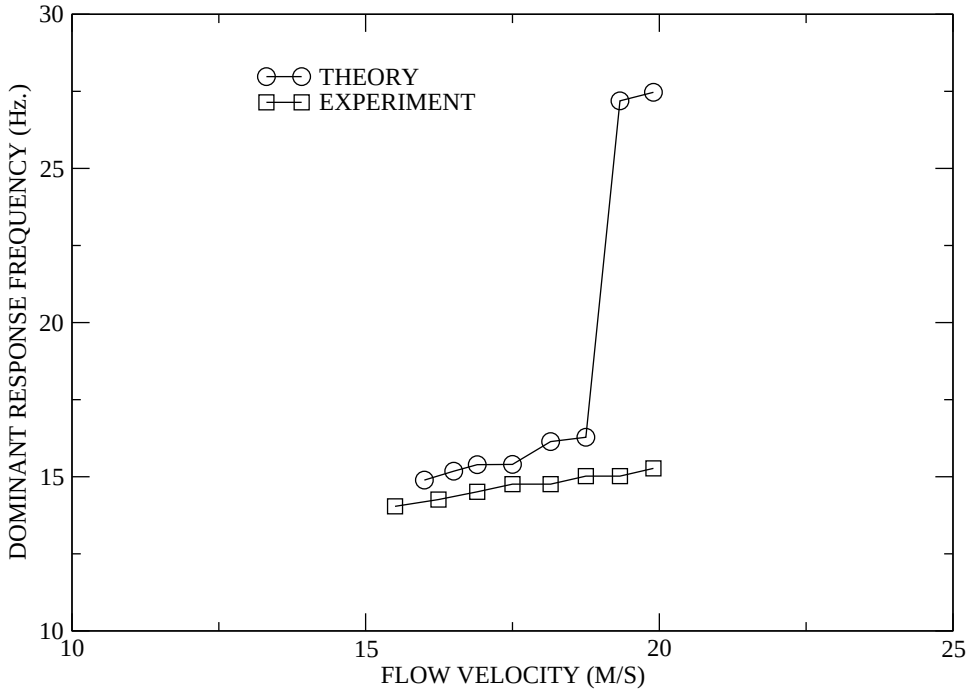

Figure 7. LCO dominant response frequency for component B trailing edge tip velocity versus flow velocity; $\theta_b = 30$**,**$\theta_c = 60$**.**

the comparison between the computation and experiment for these response frequencies is good. Also, in both the computation and experiment, the response frequencies appear to increase with increasing flow velocity. However, unlike the experiment, as the flow velocity increases, the computational model results show increasing dynamic complexity in the form of multiple frequencies having significant contributions to the response. This behavior is shown in Fig. 8 which compares the discrete Fourier transform for the computational and experimental model at a flow velocity of 19.723 m/s for the the $\theta_c = 0$ configuration. The computational results show the presence of multiple contributing response frequencies,many of which are not integer multiples of each other. This increase in dynamic complexity causes the dominant frequency to switch to a higher frequency for higher flow velocities as is seen in Figs. 5 and 6. The complex nature of the *computational* results is further shown in Figs. 9 and 10 which give the velocity response time history and phase plots for the component B tip,trailing edge location at a flow velocity of 22.70 m/s. The folding wing configuration for these two figures is $\theta_c = 0$. In contrast to Fig. 10, Fig. 11 is a phase plot for the same configuration at a flow velocity of 16 m/s which is near the flutter velocity. The differences in the nature of the phase portraits are apparent.

In order to attempt to quantify this dynamic complexity a measure has been used which is computed as the ratio of the magnitude of the maximum Fourier coefficient A_{max} to the magnitude of all of the Fourier coefficients where this latter value is computed as $\sqrt{\sum_i A_i^2}$.

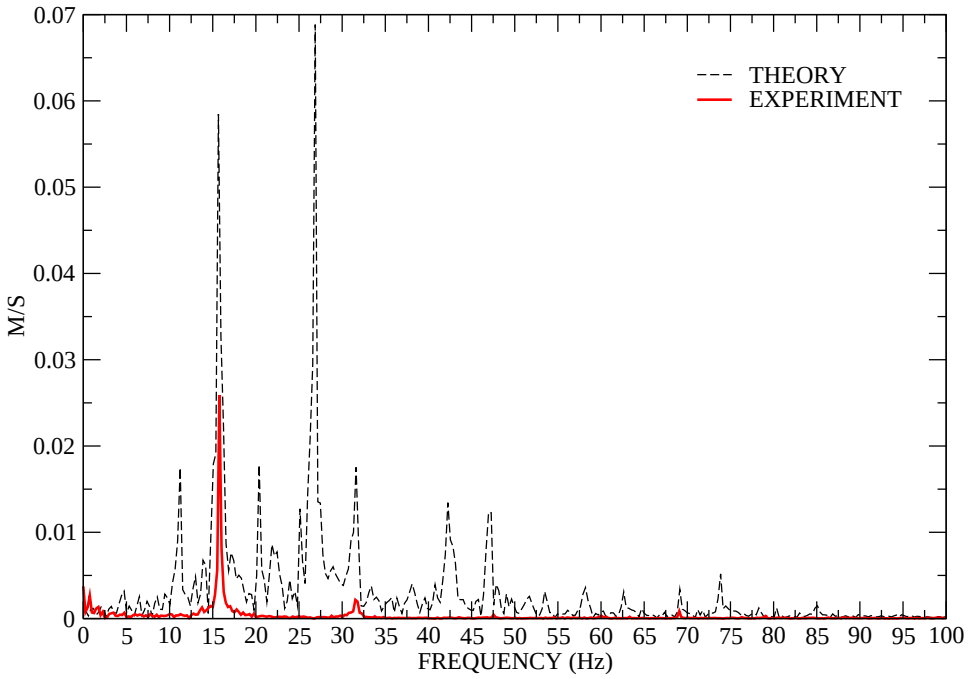

Figure 8. Discrete Fourier transform of component B trailing edge tip LCO velocity at a flow velocity of 19.723 m/s; $\theta_c = 0$.

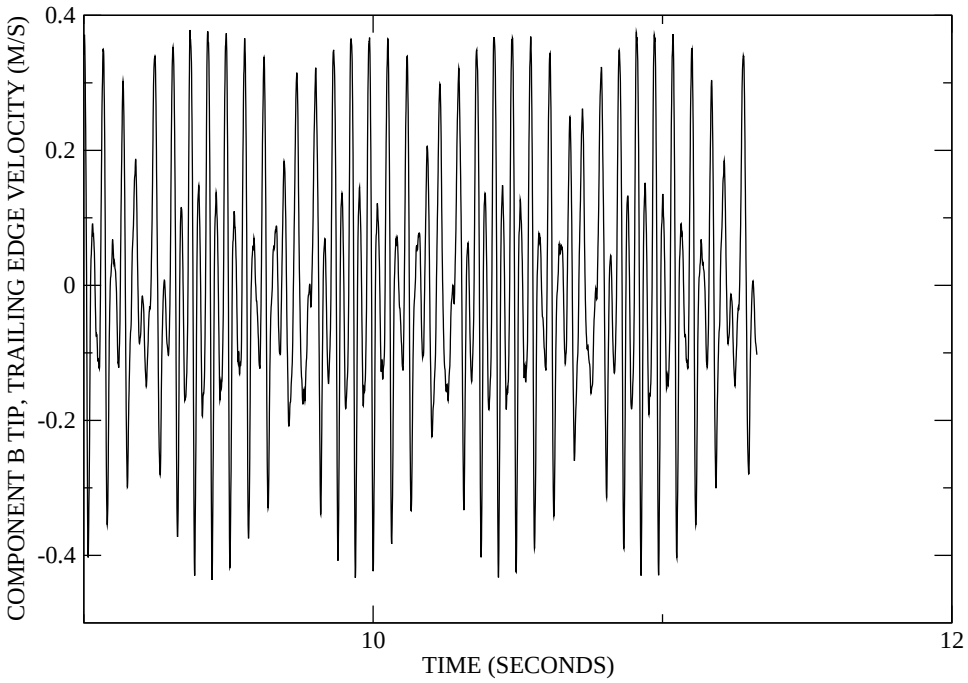

Figure 9. Component B trailing edge,tip LCO velocity versus time at a flow velocity of 22.70 m/s; $\theta_c = 0$.

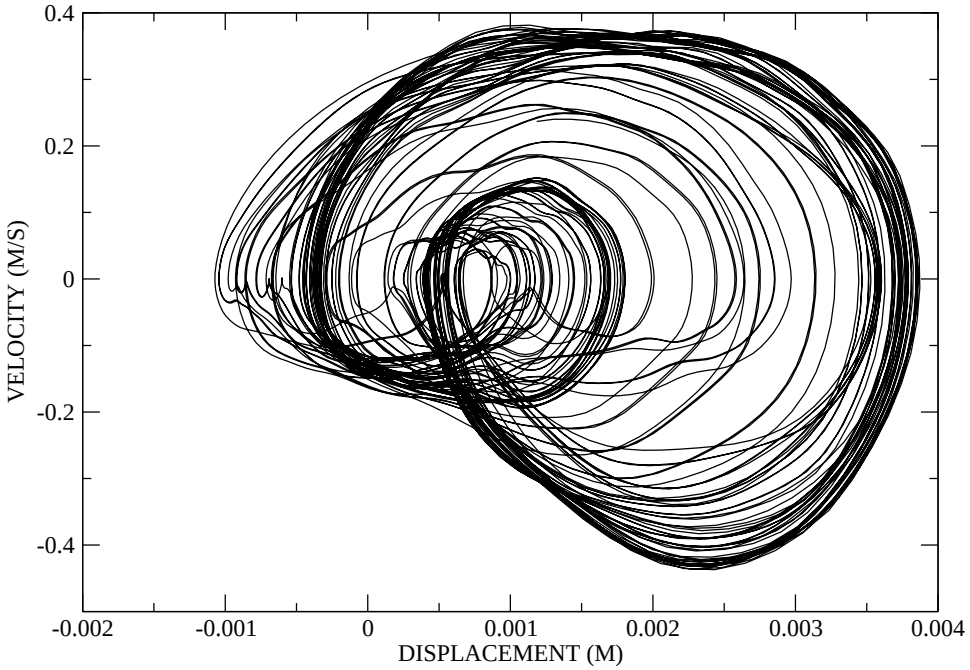

Figure 10. Component B trailing edge, tip LCO phase portrait at a flow velocity of 22.70 m/s; $\theta_c = 0$.

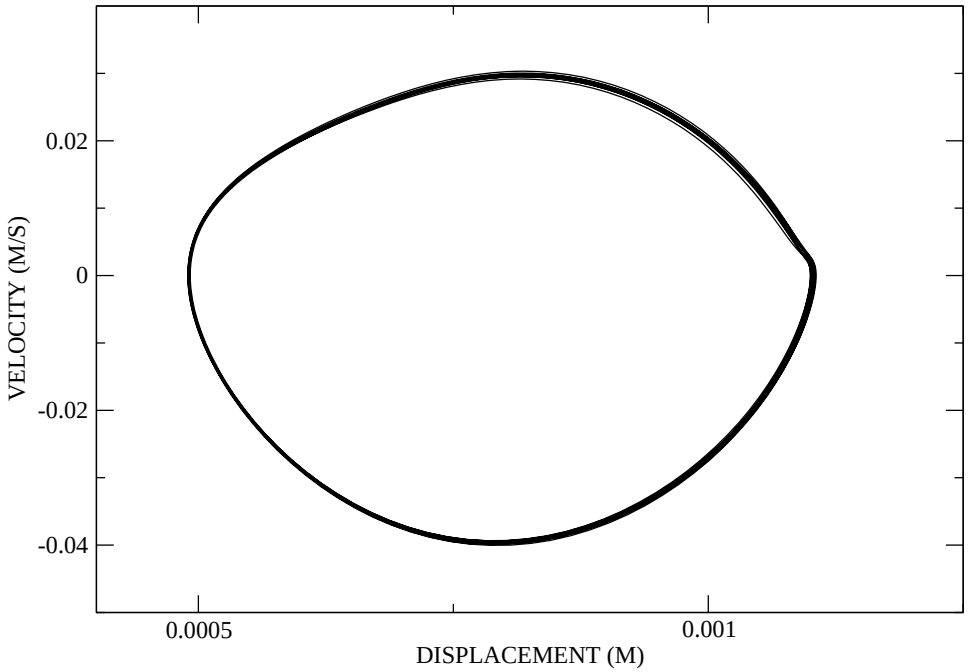

Figure 11. Component B phase trailing edge, tip LCO phase portrait at a flow velocity of 16.00 m/s; $\theta_c = 0$.

In order to account for discrete sampling the maximum and the two surrounding points are used in the computation of A_{max}. A small value of this measure denotes higher dynamic complexity in the form of more frequency components contributing significantly to the response. T l4.

As c: ow

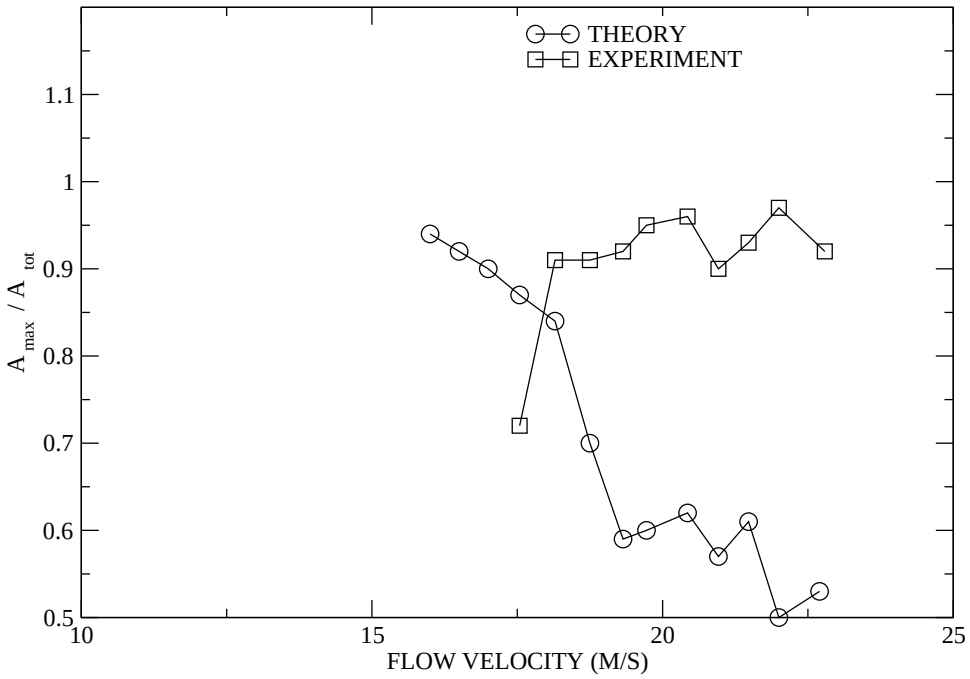

Figure 12. Component B tip,trailing edge velocity dynamic complexity measure versus flow velocity; $\theta_b = 30$,$\theta_c = 0$**.**

velocity while the experimental models appear to have mostly a single frequency response.

It is interesting that the outboard wing computational results shown in Fig. 15 do not show this trend. This figure demonstrates that for the outboard wing a single frequency response occurs over the flow velocity range investigated. Also from Fig. 16 it can be seen that the computed tip displacement of the outboard wing is quite large, especially for the two configurations with the smaller outboard wing folding angle ($\theta_c = 0$ and $\theta_c = 30$). The $theta_c = 60$ configuration shows much smaller outboard wing tip limit cycle amplitudes and a larger degree of "nonlinear stiffening" as the flow velocity is increased.

A. Conclusions

The nonlinear aeroelastic response characteristics of a three component(fuselage,inboard wing and outboard wing) folding wing configuration are investigated both experimentally and theoretically. The theoretical analysis includes a nonlinear structural dynamics model using a discrete Ritz basis derived from finite elment and component synthesis analysis and

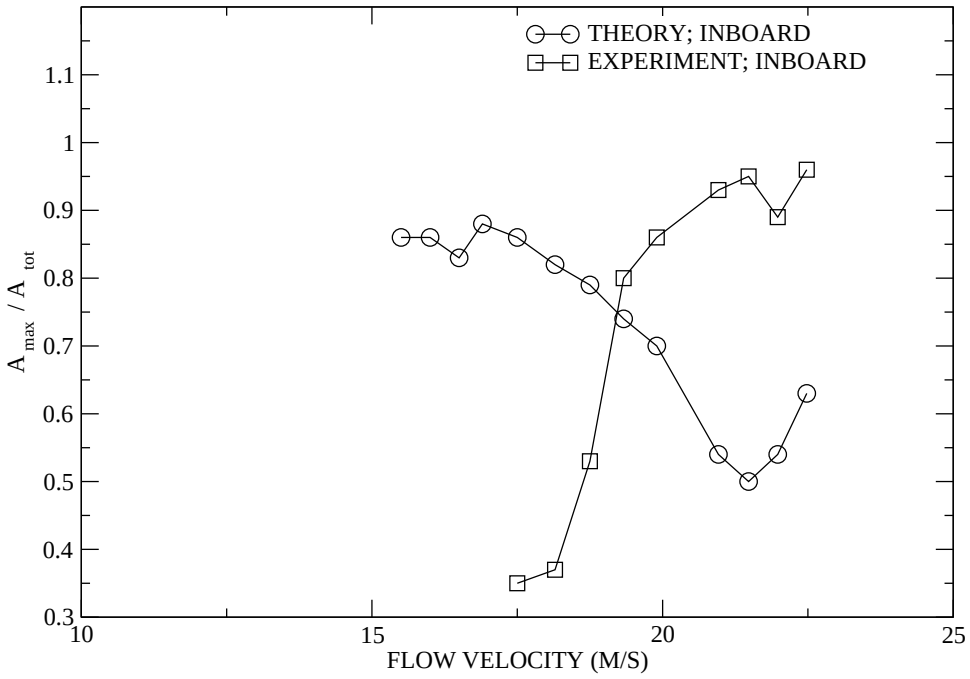

Figure 13. Component B tip,trailing edge velocity dynamic complexity measure versus flow velocity; $\theta_b = 30$**,**$\theta_c = 30$**.**

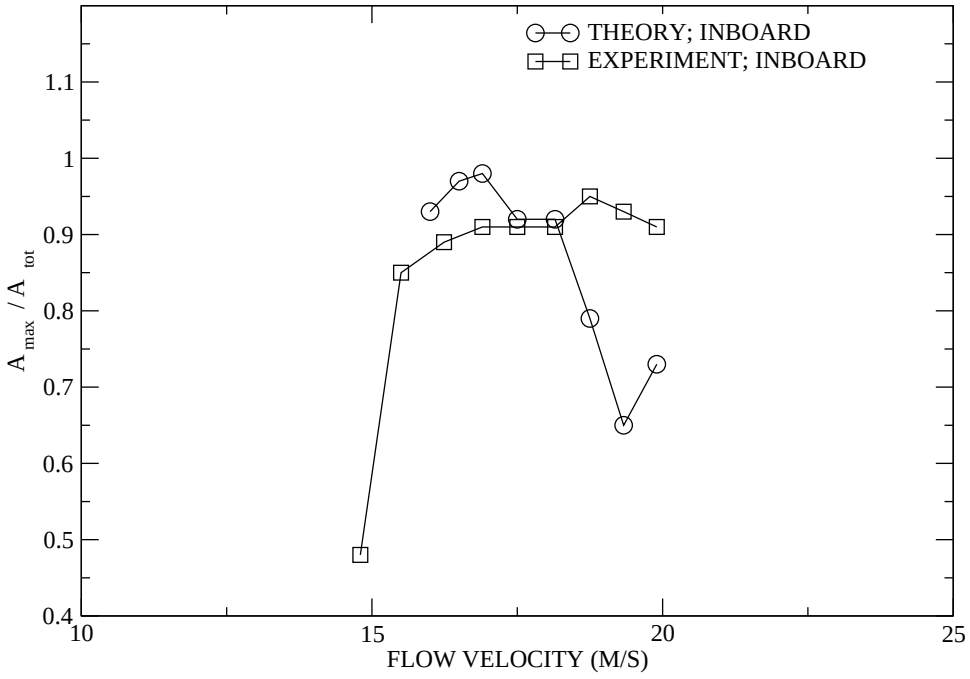

Figure 14. Component B tip,trailing edge velocity dynamic complexity measure versus flow velocity; $\theta_b = 30$**,**$\theta_c = 60$**.**

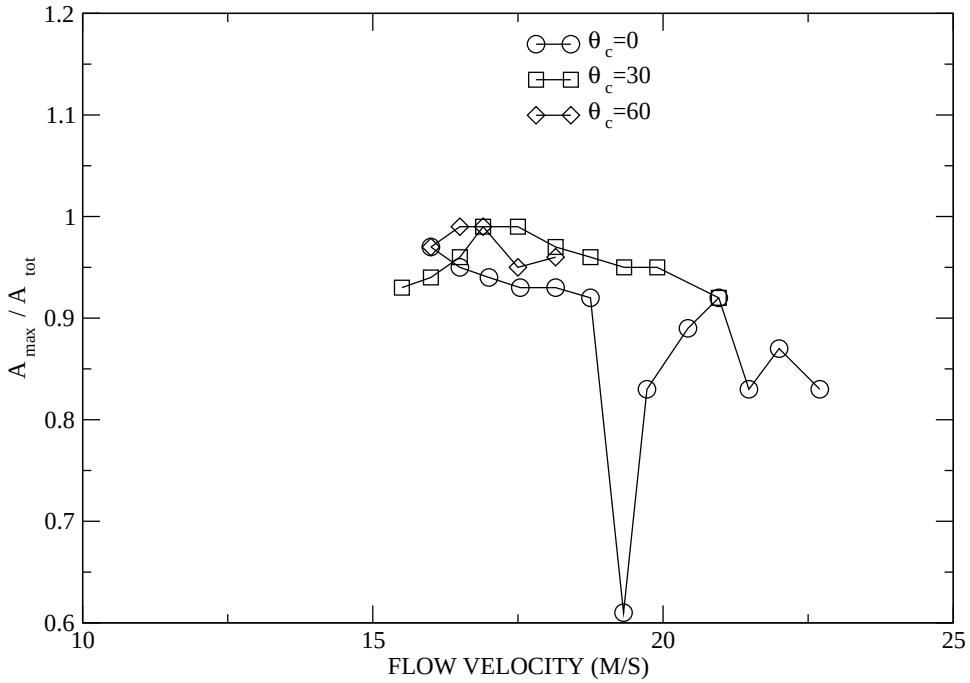

Figure 15. Theoretical component C tip, trailing edge velocity dynamic complexity measure versus flow velocity.

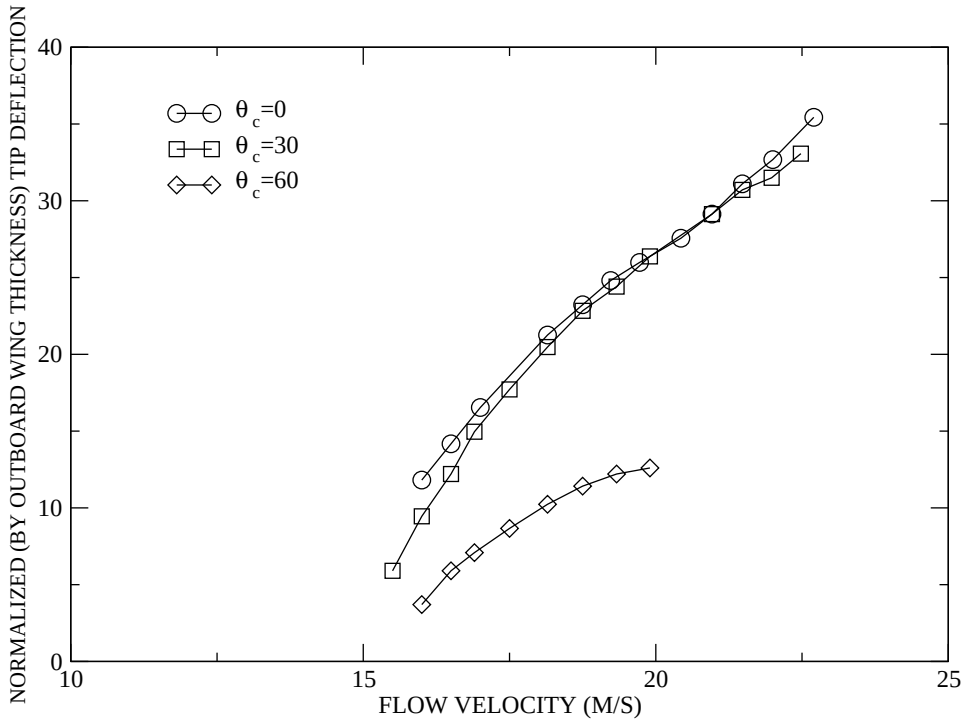

Figure 16. Theoretical component C tip, trailing edge root mean square LCO displacement versus flow velocity.

a nonlinear vortex lattice potential flow model for the fluid.

Computational results for an inboard wing folding angle of 30 degrees and three different outboard wing folding angles (0,30 and 60 degrees) are compared to experiment. For each configuration, post-flutter limit cycle oscillations are found in both the experiment and computations. Overall the correlation between the computation and experiment in this post-flutter region is good. Predicted and experimental response amplitude and frequencies for the inboard wing trailing edge tip position compare favorably. The theoretical model predicts similar outboard limit cycle tip displacements for outboard wing folding angles of 0 and 30 degrees while the configuration where the outboard folding angle is 60 degrees show signficantly smaller limit cycle amplitudes and a higher degree of nonlinear stiffening with increasing flow velocity.

A measure of dynamic complexity consisting of the ratio of the maximum Fourier coefficient amplitude to the square root of the sum of the squares of all the amplitudes is introduced. From this measure, and by inspection of the discrete Fourier transforms, time histories and phase portaits, it is found that the computational model inboard wing response contains larger contributions from multiple frequencies as compared to the experiment leading to a more complex dynamic response. The omission of structural dynamic damping or an overly simplified theoretical model of the joint dynamics is a possible explain for this discrepancy. This complex dynamic response is not predicted for the outboard wing, as the limit cycle behavior consists mostly of a single frequency, large amplitude, response.

Finally a significant result from this study is the determination that both the experiment and computation show that differences in the limit cycle behavior do exist between the various folding wing angles. Also, based upon the calculations using a linear aerodynamic model, it appears that the nonlinear aerodynamic effects are smaller than the nonlinear structural effects for the cases studied.

Acknowledgments

This work was supported under AFOSR Grant, "Nonlinear Aeroelasticity of Novel Configurations", under the direction of Dr. John Schmisseur. The first author would like to acknowledge The University of Oklahoma Supercomputing Center(OSCER) which provided supercomputing time enabling the completion of this work.

References

[1]Wlezien, R., Horner, G., McGowan, A., Padula, S., Scott, M., Silcox, R., and Simpson, J., "The Aircraft Morphing Program," AIAA 98-1927, April 1998.

[2]Wilson, J., "Morphing UAVs Change the Shape of Warfare," *Aerospace America*, Vol. 42, No. 2, Feb.

2004, pp. 28–29.

[3]Dunn, J., Horta, L., Ivanco, T., Piatak, D., Samareh, J., Scott, R., and Wieseman, C., "NASA Contributions to DARPA MAS Program," Aerospace Flutter and Dynamics Council Meeting, NASA Langley Research Center, Hampton, VA, May 2004.

[4]Snyder, M., Frank, G., and Sanders, B., "Aeroelastic Analysis of a Morphing Z-Wing Configuration," *Aerospace Flutter and Dynamics Council Meeting*, NASA Langley Research Center, Hampton, VA, May 2004.

[5]Lee, D. and Weisshaar, T., "Aeroelastic Studies on a Folding Wing Configuration," AIAA Paper 2005-1990, April 2005.

[6]Michael, B. and Kamesh, S., "Dynamic Aeroelastic Stability of Morphable Wing Structures," AIAA Paper 2006-2133.

[7]Snyder, M., Sanders, B., Eastep, F., and Frank, G., "Sensitivity of Flutter to Fold Orientation and Spring Stiffness of a Simple Folding Wing," *Proceedings of the International Forun on Aeroelasticity and Structural Dynamics 2005*, NASA Langley Research Center, Hampton, VA, June-July 2005.

[8]Lee, D. and Chen, P., "Nonlinear Aeroelastic Studies on a Folding Wing Configuration with Free-play Hinge Nonlinearity," AIAA Paper 2006-1734.

[9]Tang, D. and Dowell, E. H., "Theoretical and Experimental Aeroelastic Study for Folding Wing Structures," *Journal of Aircraft*, Vol. 45, No. 4, July-August 2008, pp. 1136–1147.

[10]Meirovitch, L., *Principles amd Techniques of Vibrations*, Prentice-Hall,Inc., Upper Saddle River,New Jersey, 1997.

[11]Crisfield, M., *Non-linear Finite Element Analysis of Solids and Structures*, Vol. 2, John Wiley & Sons Ltd, 1997.

[12]Dowell, E. H., "Free Vibrations of an Arbitrary Structure in Terms of Component Modes," *Journal of Applied Mechanics*, Vol. 39, 1972.

[13]Dowell, E. H., "Component Mode Analysis of a Simple Non-Linear Non-Conservative System," *Journal of Sound and Vibration*, Vol. 80, 1982, pp. 233–246.

[14]Dowell, E. H., "Component Modal Analysis of Nonlinear, Nonconservative Systems," *Journal of Applied Mechanics*, Vol. 50, 1983, pp. 204–209.

[15]Craig, R., *Structural Dynamics: An Introduction to Computer Methods*, Wiley, New York, 1981, Chapter 19.

[16]Castanier, M., Tan, Y., and Pierre, C., "Characteristic Constraint Modes for Component Mode Synthesis," *AIAA Journal*, Vol. 39, No. 6, 2001, pp. 1182–1187.

[17]Cook, R., Malkus, D., Plesha, M., and Witt, R., *Concepts and Applications of Finite Element Analysis*, John Wiley & Sons, New York,NY, 4th ed., 2002.

[18]Wu, S.-C. and Haug, E. J., "Geometric Non-Linear Substructuring for Dynamics of Flexible Mechanical Systems," *International Journal for Numerical Methods in Engineering*, Vol. 26, 1988, pp. 2211–2226.

[19]Dowell, E. H. and Tang, D., *Dynamics of Very High Dimensional Systems*, World Scientific Publishing Co., New Jersey, 2003.

[20]Attar, P., "Cantilevered Plate Rayleigh-Ritz Trial Function Selection for von Karman's Plate Equations," *Journal of Aircraft*, Vol. 44, No. 2, 2007, pp. 654–661.

[21]ANSYS inc., *ANSYS User Manual, Release 11.0*, 2008.

[22]Ashley, H. and Landahl, M., *Aerodynamics of Wings and Bodies*, Dover Publications Inc, New York, 1965.

[23]Katz, J. and Plotkin, A., *Low-Speed Aerodynamics*, University Press, Cambridge, 2nd ed., 2001.

[24]Attar, P., Dowell, E., and Tang, D., "Modeling Aerodynamic Nonlinearities for Two Aeroelastic Configurations: Delta Wing and Flapping Flag," AIAA Paper 2003-1402 April 7-10, 2003.

[25]Attar, P. and Gordnier, R., "Aeroelastic Modeling Using a Geometrically Nonlinear P-Version Mixed Reissner-Mindlin Plate Element," AIAA Paper 2007-2318 Presented at the 48th AIAA Structures,Structural Dynamics and Materials Conference, Honolulu, HI, April 23-26 2006.

[26]Hibbitt, H. and Karlsson, B., "Analysis of Pipe Whip," ASME Pressure Vessel and Piping Conference, San Francisco, June 25-29 1979.

[27]Hibbitt, H. and Karlsson, B., "Analysis of Pipe Whip," Tech. Rep. EPRI NP-1208, Electric Power Res. Inst., Palo Alto, November 1979.